Nanoscale Advances

ROYAL SOCIETY OF CHEMISTRY

PAPER

View Article Online
View Journal | View Issue

Cite this: *Nanoscale Adv.*, 2025, **7**, 7341

Synergistic enhancement of supercapacitor performance using covalent organic frameworks integrated with nitrogenated-reduced graphene oxide and polyaniline

Daniel Malesela Teffu,[ab] Katlego Makgopa[c] and Kwena Desmond Modibane *[ab]

The demand for advanced energy storage systems has driven research into supercapacitors and supercabatteries due to their high-power density, rapid charge–discharge capabilities, and long cycle life. This study explores the synergistic enhancement of supercapacitor performance by integrating Covalent Organic Frameworks (COFs) with nitrogen-doped reduced graphene oxide (NrGO) wrapped with polyaniline (PANI). The unique structural and electrochemical properties of COFs provide high surface area and tunable porosity, which are critical for optimizing ion transport and charge storage. Incorporating nitrogen into the rGO lattice improves electrical conductivity and enhances electrochemical performance by providing additional active sites for charge storage. The resulting composite exhibits a hierarchical structure that facilitates efficient ion diffusion and enhances capacitance. Electrochemical characterization was conducted using CV, GCD, and EIS. The electrochemical performance of the PANI-COF/NrGO composite demonstrated battery-type behaviour with a significantly increased specific capacity of 409 C g^{-1} at a scan rate of 20 mV s^{-1} in CV and 410 C g^{-1} at a current density of 2 A g^{-1} in GCD. Moreover, the full cell (two electrode system) analysis of PANI-COF/NrGO composite revealed an energy density of 9.2 Wh kg^{-1} at a power density of 300 W kg^{-1}, with a 60% capacitance retention after 5000 cycles, indicating excellent durability. This study provides valuable insights into the design of high-performance supercapacitors by utilizing the synergistic effects of COFs, NrGO, and PANI. The findings highlight the potential of the PANI-COF/NrGO composite material for applications in energy storage devices, paving the way for future developments in sustainable energy solutions.

Received 20th July 2025
Accepted 30th September 2025

DOI: 10.1039/d5na00698h

rsc.li/nanoscale-advances

1. Introduction

The demand for efficient and sustainable energy storage devices is rapidly increasing due to the growing use of intermittent renewable energy sources (such as solar and wind energy).[1,2] Energy storage devices, including Supercapacitors (SCs), are essential for storing excess energy when production exceeds demand and ensuring a reliable supply of energy, even when renewable energy sources are not actively producing sufficient power.[3,4] SCs have emerged as promising devices for bridging the gap between conventional capacitors and batteries.[5] However, the currently used electrode materials often produce limited or relatively low energy density, which restricts their widespread adoption in large-scale applications.[6]

To overcome this limitation, significant efforts in research have been devoted to the development and improvement of advanced electrode materials that can enhance energy storage performance.[7] However, the effectiveness of current SC technologies is constrained by the limitations of conventional electrode materials (*i.e.*, EDLCs and pseudocapacitive electrode materials), making the search for novel battery-type alternatives essential.[8,9] A combination of materials with complementary properties, such as high surface area, electrical conductivity, and redox activity, can lead to the development of advanced hybrid electrode materials.[10–12]

Porous electrode materials such as Covalent Organic Materials (COFs) and Metal Organic Frameworks (MOFs) with high specific surface areas and sufficient electroactive sites are believed to produce enhanced electrochemical performance due to their porous nature, which is linked to the transportation of ions, thereby resulting in improved specific capacitances.[13] COFs have recently gained attention as a novel class of materials

[a]*Department of Chemistry, School of Physical and Mineral Sciences, University of Limpopo (Turfloop), Polokwane, Sovenga 0727, South Africa. E-mail: kwena.modibane@ul.ac.za*

[b]*DSI-NRF SARChI Chair in Photoelectrocatalytic Hydrogen Production, University of Limpopo (Turfloop), Polokwane, Sovenga 0727, South Africa*

[c]*Department of Chemistry, Faculty of Science, Tshwane University of Technology (Acardia Campus), Pretoria 0001, South Africa*

for energy storage applications because of their unique structural characteristics, such as high surface area, tunable pore sizes, and excellent chemical stability. These properties make COFs ideal candidates for enhancing the electrochemical performance of energy storage devices.[14] Pristine COFs employed as SCs or supercapattery electrodes have been well documented.[15–17] However, COFs often face limitations in conductivity, which can hinder their practical applications, and this limitation mainly arises from their insulating organic backbones, which restrict charge carrier mobility and impede efficient electron transport across the framework.[18] To tackle these challenges, hybridizing COFs with other conductive materials presents a promising strategy. Carbon materials such as reduced graphene oxide (NrGO) and conductive polymers like polyaniline (PANI) are two key candidates for enhancing the electrochemical performance of COF-based composites.[19] NrGO provides an excellent conductive backbone that facilitates rapid electron and ion transport, while PANI, a conducting polymer, boosts overall capacitance through its redox–active properties.[20]

Several studies have reported improved electrochemical performance by combining COFs or PANI with graphene-based support. For example, Peng *et al.*,[21] developed an electrode material using a composite of three-dimensional porous kenaf stem-derived carbon (3D-KSC), COF-LZU1, and polyaniline (PANI). COF-LZU1 was synthesized through a condensation reaction and uniformly attached to the inner walls of 3D-KSC, enhancing structural stability. PANI was then polymerized on this structure *via* chemical oxidation. Characterization techniques, such as SEM, FTIR, and Raman spectroscopy, were employed to confirm the successful synthesis and uniform distribution of the components. The resulting 3D-KSC/COF-LZU1/PANI composite showed a high specific capacitance of 583.0 mF cm^{-2} at 0.1 mA cm^{-2}, retaining 81.5% of its capacity after 2000 cycles, indicating excellent electrochemical performance and the promise of COF and PANI-based composites as electrode materials for Sc applications. Nevertheless, a rationally designed triple hybrid system that integrates PANI with COF/NrGO has not yet been systematically investigated. Such an approach is expected to synergistically combine the unique merits of each component for enhanced performance.[22]

Herein, we report a novel PANI-COF/NrGO composite designed to synergistically integrate the structural versatility of COFs, the conductivity of NrGO, and the pseudocapacitance of polyaniline. This unique tri-component hybrid is engineered to overcome the intrinsic limitations of COFs and graphene derivatives, offering a pathway toward improved specific capacitance, energy density, and cycling stability. To our knowledge, this is among the first studies to comprehensively evaluate COF/NrGO-based composites in supercapacitors, supported by morphological, thermal, and electrochemical analyses. This work not only demonstrates a promising electrode material but also provides insights into interface engineering for next-generation energy storage devices.

2. Experimental section

2.1. Chemicals and materials

Aniline ($C_6H_5NH_2$), trimesic acid (1,3,5-benzenetricarboxylic acid), potassium hydroxide (KOH), Iron chloride ($FeCl_3$), polyvinylidene fluoride binder (PVD binder), *N*-methyl pyrrolidone (NMP), graphite powder (C), melamine ($C_3H_6N_6$), nickel foam (NF), carbon black, activated carbon (AC), and ammonium persulfate ($(NH_4)_2S_2O_8$) were obtained from Sigma-Aldrich (South Africa). Sulfuric acid (H_2SO_4), dimethylformamide (DMF), hydrogen peroxide (H_2O_2), and dimethyl sulfoxide (DMSO) were purchased from Rochelle Chemicals (South Africa). SAARCHEM (South Africa) supplied hydrochloric acid (HCl) and potassium permanganate ($KMnO_4$), while Moncon (South Africa) supplied hydrogen peroxide (H_2O_2). Sodium nitrate ($NaNO_3$) was purchased from Riedel-de Haen.

2.2. Synthesis of COF/NrGO and PANI-based composites

The melamine-based COF was synthesized using a previously used method.[23] NrGO was prepared using the modified Hummers' method.[24] COF/NrGO composite was produced by the impregnation method.[25] In brief, 0.1 g of the COF sample was suspended in 10 mL of DMSO. In a separate beaker, 0.1 g of NrGO was dispersed in 1.4 mL DMSO, and then the two mixtures were mixed and stirred magnetically for 24 hours at room temperature. The resulting product was recovered by filtration and washed with ethanol and then dried overnight at 50 °C.

The PANI-based composites were prepared using the *in situ* polymerization of aniline in the presence of the previously prepared materials (*i.e.*, either COF, NrGO, or COF/NrGO). In brief, 1 mL of the aniline monomer and 3.6 wt% of the materials (COF, NrGO, or COF/NrGO) were dissolved in a 1 : 10 solution of H_2O and HCl in a 250 mL round-bottom flask. The solution was stirred for 30 min and kept at 50 °C. About 2.40 g of $(NH_4)_2S_2O_8$ and 1.88 g of $FeCl_3$ were added to the solution. The reaction mixture was stirred for an additional 3 hours at the same temperature. The mixture was placed in an oven overnight to evaporate the solvents; the remaining content was washed with ethanol several times and re-dried at 50 °C (Scheme 1).[26]

2.3. Electrode preparation

The preparation of electrodes was carried out according to the literature. A NF with a 1 cm^2 area was soaked in 1 mol L^{-1} HCl and ultrasonicated for 15 minutes to remove the nickel oxide

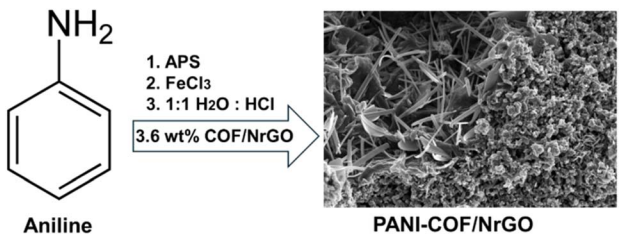

Scheme 1 Synthesis scheme for PANI-COF/NrGO composite.

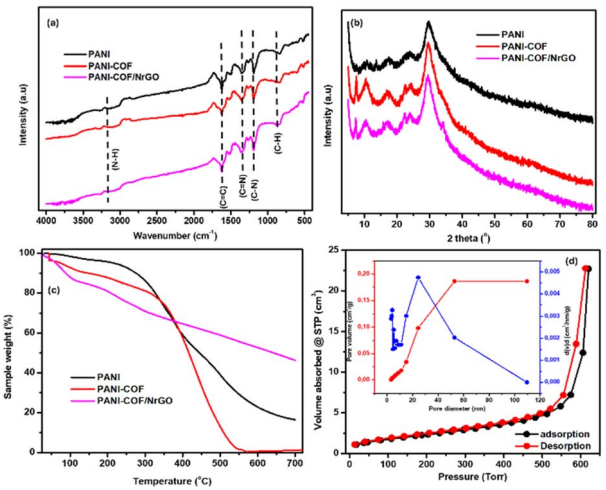

Fig. 1 (a) FTIR patterns of PANI, PANI/COF, and PANI-COF/NrGO composite, (b) XRD patterns of PANI-COF and PANI-COF/NrGO, (c) TGA spectrum of PANI, PANI-COF, and PANI-COF/NrGO, (d) N_2 adsorption–desorption isotherms for PANI-COF/NrGO.

layer. The electrodes were then ultrasonicated in a mixture of deionized water and ethanol for an additional 15 minutes. The NF electrodes were further pressed at high pressure to close the pores in their structure before coating. The electrodes consisted of three different materials: 70% of the synthesized materials (PANI, PANI-COF, and PANI-COF/NrGO composite), 20% carbon black material (used to enhance capacitance), and 10% binder (PVDF). The materials were mixed and crushed before being saturated with NMP to form a sludge, which was coated on the NF current collector. The prepared electrodes were dried for 12 hours at 50 °C. The coated materials averaged a mass loading of 5 mg. 3 mol L^{-1} KOH solution was prepared in a 250 mL volumetric flask and used as an electrolyte. CV, GCD, and EIS measurements were used to evaluate the electrochemical properties of the materials. A three-electrode setup was used for electrochemical characterization, where active material was coated onto nickel foam to serve as the working electrode, Ag/AgCl as the reference electrode and platinum wire as the counter electrode. The two-electrode supercapacitor device was assembled using a split cell with AC as the anode and a PANI-COF/NrGO composite as the cathode. A membrane was used as a separator, and 3 mol L^{-1} electrolyte was employed.[27] All tests were performed at room temperature.

2.4. Electrode material characterization

The successful synthesis of PANI, PANI-COF, and PANI-COF/NrGO ternary composites was confirmed using an FTIR-TGA hybrid system (Spectrum II PerkinElmer). The analysis was conducted at room temperature over a wavenumber range of 4500 to 400 cm^{-1}. The structure of the prepared powder samples was examined with a Malvern Panalytical Aeris diffractometer, equipped with a PIXcel detector and fixed slits, using Fe-filtered Co-Kα radiation. Thermal analysis was carried out using a PerkinElmer STA 6000 instrument connected to a PolyScience digital temperature controller under a nitrogen environment with a flow rate of 20 mL min^{-1}. Samples weighing from 30 mg were heated from 30 to 800 °C at a steady rate of 10 °C min^{-1}. Data were collected and analyzed with Pyris software®. The surface morphology of the samples was observed using a field-emission scanning electron microscope (FE-SEM, Auriga Carl Zeiss) operated at 30 kV. The FE-SEM was integrated with an energy-dispersive spectroscopy (EDS) elemental analyzer. Nitrogen adsorption–desorption isotherms were obtained using a NOVA 800 instrument (St 4 module) through N2 adsorption and desorption. Degassing was performed under vacuum, raising the sample temperature to 150.0 °C at a rate of 5 °C min^{-1}, then maintained for 240 minutes. Electrochemical measurements were performed in a temperature-controlled laboratory using a Biologic potentiostat (VMP300) and EC-Lab software.

3. Results and discussion

3.1. Structural characterization

Fig. 1(a) shows the FTIR spectra of PANI, PANI-COF, and PANI-COF/NrGO. The FTIR spectra of all the prepared materials were similar to the spectrum of PANI, with varying peak intensities.[28] This is attributed to the wrapping of the synthesized materials with the PANI around their surfaces. The main characteristic peak of PANI was observed as a broad peak at around 3200 cm^{-1}, which is ascribed to the N–H stretching 29. The peak at 3000 cm^{-1} was assigned to the aromatic C–H stretching, and the band at around 2840 cm-1 was due to the stretching vibration of the methyl group. The benzenoid and quinoid rings of the polyaniline ring were represented by the peaks around 1490 and 1570 cm^{-1}, respectively. The peak at 1375 cm^{-1} was attributed to the C–N stretching connecting the quinoid and the benzenoid 30. The peak at 1105 cm^{-1} was attributed to the aromatic C–H bending in the plane for the 1,4-disubstituted aromatic ring, and the band appearing at 830 cm^{-1} was attributed to an aromatic C–H out-of-plane bending vibration 31. In the PANI-COF spectrum, the COF contribution is evident

Table 1 XRD parameters for PANI, PANI-COF, and PANI-COF/NrGO composite

Material	CI (%)	D (nm)	Strain ($\times 10^{-3}$)	Dislocation density ($\times 10^{16}$ m^{-2})	d (Å)	R (Å)
PANI	56.25	5.48	6.32	3.32	2.97	3.72
PANI-COF	68.58	4.69	7.38	4.53	2.99	3.74
PANI-COF/ NrGO	78.39	6.08	5.69	2.70	3.00	3.75

Table 2 BET results summary of COF, NrGO, and PANI-COF/NrGO composite

	Surface area ($m^2\ g^{-1}$)	Pore volume ($cm^3\ g^{-1}$)	Pore diameter (nm)	Isotherm and pore types
COF	142.09	0.588	11.19	Type IV, mesopores
NrGO	12.33	0.0191	3.63	Type IV, mesopores
PANI-COF/NrGO	33.11	0.186	24.48	Type IV, mesopores

from additional absorptions around 1650 cm^{-1} (C═O stretching) and 1240–1260 cm^{-1} (C–N stretching), indicating the preservation of the imine-linked COF backbone within the composite. The overlap of these peaks with those of PANI confirms chemical compatibility and composite formation 32. Finaly, the ternary composite spectrum further validates the successful integration of NrGO. The small absorption features in the range 1720–1740 cm^{-1} correspond to C═O stretching of oxygenated groups in NrGO. The incorporation of NrGO is also evidenced by the broadening of bands in the region of 1000–1300 cm^{-1}, which can be attributed to overlapping C–O and C–N vibrations. Importantly, the spectral changes, including peak shifts, broadening, and slight intensity variations, confirm strong interfacial interactions and successful formation of the PANI-COF/NrGO ternary composite.[33]

Fig. 1(b) shows the XRD analysis of PANI-COF and PANI-COF/NrGO. The PANI-COF curve showed a distinctive broad peak is observed around $2\theta = 26°$, which corresponded to the (002) plane as the presence of the π–π stacking interactions between the conjugated aromatic systems in the COF and PANI chains.[34] Additional broad features below $2\theta = 20°$ were also evident, which were attributed to the intrinsic structural disorder within the hybrid framework. In contrast, the PANI-COF/NrGO composite exhibited a noticeable reduction in the intensity and broadening of the diffraction peak around $2\theta = 26°$, along with a shift to slightly lower angles. This attenuation and broadening were indicative of reduced structural ordering, likely due to the intercalation and partial exfoliation of NrGO layers within the PANI-COF matrix. The incorporation of NrGO disrupted the π–π stacking and interlayer ordering, which was reflected in the diminished crystallinity. The shift to lower angles suggests an increased interlayer spacing, possibly arising from the interaction between the NrGO nanosheets and polymeric chains or COF segments. On the other hand, the degree of crystallinity index (CI, %) was calculated from the ratio of crystalline peak area to total peak area. The percentage crystallinity of PANI, PANI-COF, and PANI-COF/NrGO, as determined from the plots, were around 56.25%, 68.58% and 78.39%, respectively (see Table 1). The higher the degree of regularity in the arrangement and ordering of the polymer chains, the higher the crystallinity as observed in PANI-COF/NrGO composite due to the presence of COF and NrGO dopant. The *d*-spacing (*d*) of the highest intense crystalline peak was calculated by the Debye–Scherrer method using Bragg's relation.[35] The calculated values of *d*-spacing values are presented in Table 1. The *d* value was small in the PANI, highest for PANI-COF/NrGO, and in between for PANI-COF. This indicated that the polymer chains in PANI crystals were the most compact, followed by the least compact in PANI-COF/NrGO and intermediate in PANI-COF, due to the doping effects of COF and NrGO. In addition, the crystallite size (*D*) of the highest-intense crystalline peak was also determined from the Scherrer relation.[36] The increase in crystallite size was observed in PANI-COF/NrGO composite as an indication for the reduction of grain boundaries, which helps improve electrical conductivity, charge transport, structural stability by minimizing defects, and better long-term cycling stability.[37] The *D* value was in the following order: PANI-COF/NrGO > PANI > PANI-COF. This crystallite size trend was due to the relatively higher inter-chain separation and *d*-spacing (see Table 1) for PANI-COF/NrGO compared to PANI, which showed that the polymer chains in PANI-COF/NrGO were more oriented but less compact. The reason for the high interchain separation in PANI-COF/NrGO can be related to the presence of strong inter-chain H-bonding through COF/NrGO groups, as well as the planar graphene sheets which facilitate π–π interactions with PANI chains, promoting their alignment and stacking.[38] The decrease in crystallite size can further be attributed to the COF acting as a nucleation inhibitor (due to its rigid, porous framework) limiting the growth of large PANI domains by providing multiple nucleation sites and steric hindrance, which favours the formation of smaller, more dispersed crystallites.[39] This was supported by the strain and dislocation density as given in Table 1. The PANI-COF/NrGO showed to have a small strain and dislocation density values as compared to PANI, which was in agreement with the degree of crystallinity.

The TGA analysis was used to evaluate the thermal stability of the prepared materials (*i.e.*, PANI, PANI-COF, and PANI-COF/NrGO composite), and their thermograms are presented in Fig. 1(c). The thermogram of pristine PANI revealed a two-step degradation pattern. The initial minor weight loss observed below 100 °C was attributed to the evaporation of physically adsorbed moisture. The major weight loss occurring between 250 °C and 500 °C was ascribed to the thermal degradation of the polyaniline backbone and the elimination of dopant species. The PANI-COF composite displayed an enhanced thermal profile compared to pristine PANI. Similar to PANI, the initial weight loss below 100 °C was due to moisture removal. However, a significant degradation step was observed starting around 350 °C, corresponding to the decomposition of both the PANI chains and the covalent COF network. Notably, the residue retained at higher temperatures was slightly greater than that of PANI, suggesting enhanced thermal resistance imparted by the COF matrix. Among the three materials, the PANI-COF/NrGO composite demonstrated the highest thermal stability. The onset of degradation occurred at a comparatively higher

temperature, and the rate of weight loss was more gradual throughout the heating range. This improved thermal performance was attributed to the synergistic interaction between the NrGO, COF, and PANI components. The highly stable carbonaceous nature of NrGO, combined with the structural integrity of the COF and the conducting PANI chains, contributed to the significant retention of mass beyond 600 °C. The high residual weight confirmed the robust thermal characteristics of the composite, making it suitable for applications involving high-temperature processes or prolonged operational durability.

The BET analysis was performed to determine the textural properties of PANI-COF/NrGO composite as shown in Fig. 1(d). The summarized BET data for pristine COF, NRGO, and the PANI-COF/NrGO composite are displayed in Table 2. The adsorption–desorption isotherms (Fig. 1(d) revealed a characteristic Type IV hysteresis loop, indicative of a mesoporous structure based on IUPAC classification. The presence of a distinct hysteresis between the adsorption and desorption branches further confirmed the existence of capillary condensation within mesopores and a specific surface area of 33.11 m^2 g^{-1}, which is higher than that of NrGO (12.33 m^2 g^{-1}) but less than COF (142.09 m^2 g^{-1}). This reduction can be attributed to the deposition of PANI within the COF pores and the wrapping of COF particles by NrGO sheets. The polymer chains of PANI partially occupy the COF's porous framework, while the flexible NrGO sheets cover external surfaces and interconnect COF particles, resulting in partial pore blockage.[40] The inset figure (Fig. 1(d): insert) showed the Barrett–Joyner–Halenda (BJH) pore size distribution curve, which showed that the PANI-COF/NrGO ternary composite possessed a narrow distribution of mesopores with a pore volume of 0.186 cm^3 g^{-1} and a high pore diameter of 24.48 nm. The peak centered within the mesopore range (2–50 nm) indicated uniform pore sizes, likely facilitating enhanced ion transport and diffusion pathways in electrochemical applications. The observed surface area and porosity are crucial for understanding the charge storage capabilities of the synthesized materials in SCs.

3.2. Morphological characterization

The structural integrity, surface texture, and full morphology of the synthesized samples were thoroughly examined using SEM, as shown in Fig. 2. Fig. 2(a) displays the SEM micrograph of pristine PANI, which reveals a distinct tubular or wire-like morphology characteristic of the conductive polymer. These tubular structures provided improved surface area, which is advantageous for electrochemical applications due to enhanced electrolyte/electrode interaction. This was supported by the EDS spectrum in Fig. 2(b), revealing the presence of carbon and oxygen. Chlorine, sulphur, and iron may be from the building materials of the PANI.[41] The polymerization of aniline in the presence of COF to form PANI-COF composite displayed a notable transformation in morphology, as displayed in Fig. 2(c).[19] The surface became rougher and more textured, confirming the successful embedding or coating of PANI on the COF matrix. The EDS spectrum (Fig. 2(d) showed an increment

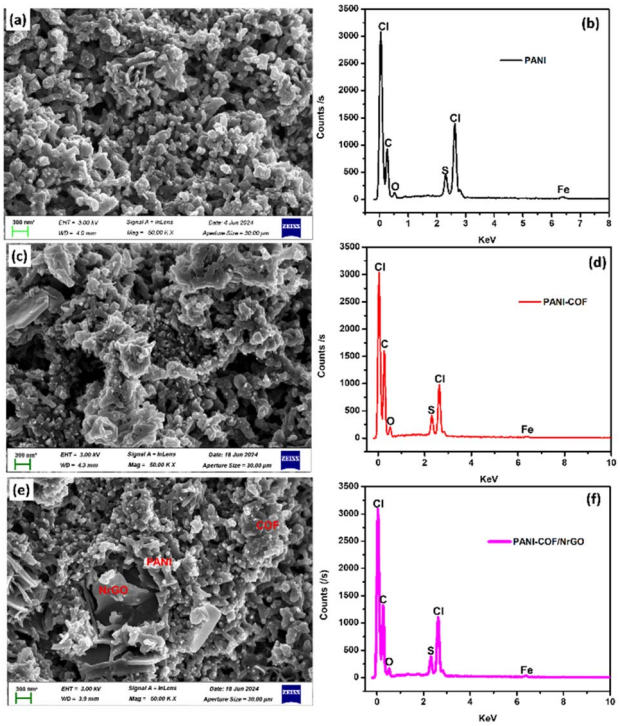

Fig. 2 SEM images of (a) PANI, (c) PANI-COF, (e) PANI-COF/NrGO. EDS spectrum of (b) PANI, (d) PANI-COF, (f) PANI-COF/NrGO.

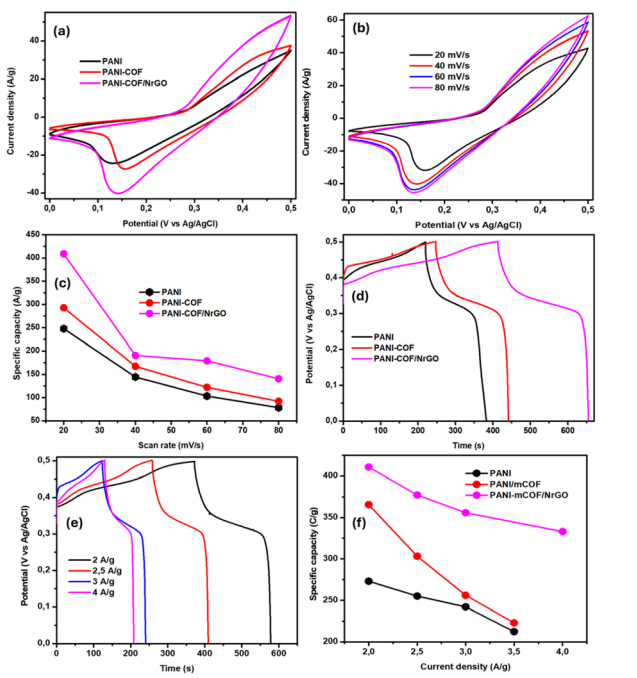

Fig. 3 (a) Comparison CV curves of PANI, PANI-COF and PANI-COF/NrGO at scan rate of 40 mV s^{-1}, (b) CV curves of COF/NrGO at different scan rates, (c) specific capacities of the PANI, PANI-COF, and PANI-COF/NrGO composite at various scan rates, (d) comparison GCD curves of PANI, PANI-COF and PANI-COF/NrGO at a current density of 2.5 A g^{-1}, (e) GCD curves of PANI-COF/NrGO at different current densities, (f) specific capacities of the PANI, PANI-COF, and PANI-COF/NrGO composite at various current densities.

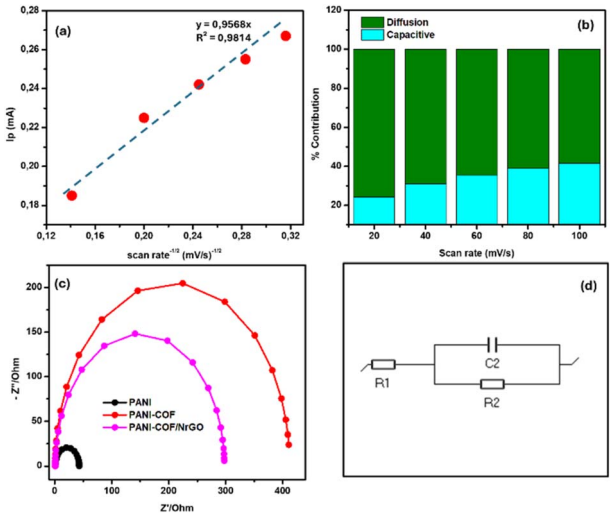

Fig. 4 (a) peak current (I_p) *vs.* $\sqrt{\text{scan rate}}$ Curve for the PANI-COF/NrGO composite, (b) percentage contributions of the diffusion and capacitive processes at different scan rates, (c) fitted EIS curves of PANI, PANI-COF, and PANI-COF/NrGO composite, (b) circuit used for fitting the EIS data.

of the atom percentage of carbon and oxygen due to the doping with COF. The morphological features of the ternary PANI-COF/NrGO composites are presented in Fig. 2(c). The image demonstrated the presence of COF particles deposited on the NrGO sheets, forming a hybrid architecture and further encapsulated or wrapped by PANI nanotubes, which interlinked across the NrGO sheets as supported by the EDS spectrum (Fig. 2(f)). This interconnected structure enhanced both mechanical integrity and electronic conductivity. The uniform dispersion of COF and the tubular PANI throughout the NrGO network indicated the formation of a well-integrated composite with potential for synergistic electrochemical behaviour.[42]

3.3. Electrochemical evaluation of the prepared materials

3.3.1. Three-electrode evaluation. The electrochemical performance of PANI, PANI-COF, and PANI-COF/NrGO composites were systematically investigated using a three-electrode setup, and the results obtained from CV, GCD (at a potential of 0.5 V *vs.* Ag/AgCl), and EIS offer critical insights into the storage behavior and rate performance of the different electrode materials. The measurements were performed on NF in 3 mol L^{-1} KOH solution. The overlaid CV curves of PANI, PANI-COF, and PANI-COF/NrGO at a scan rate of 40 mV s^{-1} are displayed in Fig. 3(a). All the prepared materials exhibited redox peaks typical of battery-type storage behaviour. Notably, the area of the CV curve for PANI-COF/NrGO was significantly larger than that for PANI and PANI-COF, indicating that the introduction NrGO enhanced the charge storage capacity of PANI-COF. Fig. 3(b) shows the CV curves of PANI-COF/NrGO at scan rates ranging from 20 to 100 mV s^{-1} within a positive potential range of 0 to 0.5 V. The redox peak in the CV curves increased with increasing scan rate, signifying that the low resistance of the interfacial composite material enhanced ionic accessibility and facilitated rapid electron transfer. Nonetheless, at higher scan rates, the redox peaks began to diminish, which was attributed to the polarization of the electrode material.[43] The specific capacities of the PANI-COF/NrGO composite, calculated using the CV curves, were obtained to be 409.79, 190.69, 179.20, and 140.44 C g^{-1} at scan rates of 20, 40, 60, and 80 mV s^{-1}, respectively, as indicated in Fig. 3(c). The specific capacities were determined from the CV data, using the eqn (1):

$$Q_S = \frac{\int I\,dV}{m \times \nu \times \Delta V} \quad (1)$$

where Q_s is the specific capacity in C g^{-1}, I is the current in mA, m is the active mass in mg, ν is the scan rate in mV s^{-1} and V is the potential window.

Fig. 3(d) represents the overlaid GCD results of the prepared electrode materials (PANI, PANI-COF, and PANI-COF/NrGO) at a current density of 2.5 A g^{-1}. The charge–discharge profiles of the materials were non-linear, indicating good reversibility of the redox reactions and confirming the battery-type capacitive characteristics as a key feature for their performance. Amongst the prepared materials, the PANI-COF/NrGO ternary composite exhibited the longest discharge time, which usually results in the highest specific capacity. Fig. 3(e) shows the charge–discharge curves of the ternary composite at different current densities, and the highest discharge time of 328.6 s was obtained at a current density of 2 A g^{-1}. The GCD results confirmed that PANI-COF/NrGO offered the best capacitance performance, which agreed with the CV results presented in Fig. 3(b). At current densities of 2, 2.5, 3, and 4 A g^{-1}, the specific capacitance values were 410.8, 377.28, 355.88, and 333.05 C g^{-1}, respectively (as indicated in Fig. 4(f)). The highest specific capacity of 410.8 C g^{-1}, which was higher than previously reported COF and PANI-based electrode materials, as

Table 3 Comparison of the PANI-COF/NrGO composite with other reported electrode materials in a three-electrode system

Electrode material	Current density (A g^{-1})	Specific capacity/capacitance	electrolyte	Potential range (V)	Ref.
rGO@PANI	1.0 A g^{-1}	314.2 F g^{-1}	3 mol L^{-1} KOH	0.8	45
TpPa-COF@PANI	0.2 A g^{-1}	95 F g^{-1}	1 mol L^{-1} H_2SO_4	0.7	46
TFP-COF	2.0 A g^{-1}	291.1 F g^{-1}	1 mol L^{-1} KOH	1.1	47
NWNU-COF-4	0.3 A g^{-1}	133.44 F g^{-1}	6 mol L^{-1} KOH	0.5	48
Pani/rGO	2.4 A g^{-1}	261 F g^{-1}	1 mol L^{-1} H_2SO_4	1.0	49
PANI-COF/NrGO	2.0 A g^{-1}	410.8 C g^{-1}	3 mol L^{-1} KOH	0.5	This work

shown in Table 3. The specific capacities from the GCD data were determined using eqn (2):

$$Q_s = \frac{I \times \Delta t}{m} \quad (2)$$

where Q_s is the specific capacity in C g^{-1}, I is the discharge current in mA, Δt is the discharge time in s, and ΔV is the potential window.[44]

The diffusion coefficient, D, was determined to understand the diffusion-controlled electron transfer of the PANI-COF/NrGO ternary composite using the Randles–Ševćik equation (eqn (3)):

$$I_P = 2.65 \times 10^5 n^{1.5} A C \sqrt{vD} \quad (3)$$

In the formula, the peak current is depicted by I_p, n is the number of electrons transferred, A is the electrode area in cm^2, D is the diffusion coefficient in cm s^{-1}, C is the bulk molar concentration of the electroactive species in mol cm^{-3}, and v is the scan rate is V s^{-1}.

The graph of peak current (I_p) *vs.* $\sqrt{\text{scan rate}}$ curve for the PANI-COF/NrGO composite is shown in Fig. 4(a), and the slope of the graph was used to calculate the diffusion coefficient of PANI-COF/NrGO ternary composite, which was calculated to be 1.55×10^{-6} cm s^{-1}.

The charge storage mechanism of the PANI-COF/NrGO composite was further elucidated by analyzing the capacitive and diffusion-controlled contributions at various scan rates, as illustrated in the percentage contribution bar chart (Fig. 4(b)). This analysis provides insight into the dominant charge storage possessed by the composite and its evolution with increasing scan rate (*i.e.*, 20 ($K_1V = 0.0178$, $K_2V^{1/2} = 0.0558$), 40 ($K_1V = 0.0356$, $K_2V^{1/2} = 0.0792$), 60 ($K_1V = 0.0534$, $K_2V^{1/2} = 0.0970$), 80 ($K_1V = 0.0712$, $K_2V^{1/2} = 0.112$) and 100 mV s^{-1} ($K_1V = 0.089$, $K_2V^{1/2} = 0.125$). At the lowest scan rates, the diffusion-controlled process is predominant, accounting for about 75% of the total charge storage. This indicates that faradaic redox reactions involving ion intercalation dominate at slower scan rates, allowing sufficient time for ions to penetrate the bulk of the electrode material. The redox kinetics become limited at higher scan rates, leading to the charge storage being increasingly dominated by rapid surface processes, which are more accessible under fast voltage sweeps. Therefore, leading to about 42% capacitive contribution at the highest scan rate.[50]

The EIS data of the synthesized materials (PANI, PANI-COF, and PANI-COF/NrGO composites) were presented in the Nyquist plot shown in Fig. 4(c). The Nyquist plots featured a typical semicircular arc in the high-to-medium frequency region. These characteristics were an indication of a charge transfer resistance-dominated process and capacitive behaviour, respectively. The diameter of the semicircle corresponds to the charge transfer resistance (R_{ct}), which provides insight into the electrical conductivity and electrochemical kinetics of the materials. Among the three materials, the PANI-COF exhibited the largest semicircle, suggesting higher charge transfer resistance. This was due to the less conductive nature of the COF framework, which hindered electron mobility across the interface. In contrast, PANI showed a reduced arc diameter compared to PANI-COF, implying enhanced conductivity owing to the intrinsically conductive nature of the polyaniline backbone. However, the most significant reduction in R_{ct} was observed for the PANI-COF/NrGO composite, which showed the smallest semicircle diameter among the samples. This result demonstrated that the incorporation of NrGO significantly improved electron transport and reduced interfacial resistance. The circuit used to fit the EIS data is shown in Fig. 4(d), and the parameters are displayed in Table 4.

Table 4 EIS parameters obtained from fitting the data in the circuit

	EIS parameters		
Material	R1 (Ohm)	C1 (F)	R2 (Ohm)
PANI	1.231	0.000782	41.743
PANI-COF	0.799	0.00226	411.365
PANI-COF/NrGO	0.923	0.00111	296.853

3.3.2. Two-electrode evaluation of the AC//PANI-COF/NrGO asymmetric device. To further assess the practical applicability of the PANI-COF/NrGO composite, an asymmetric supercapattery device was assembled using PANI-COF/NrGO as the positive electrode and activated carbon (AC) as the negative electrode, with the electrode mass loading carefully balanced according to the mass balance eqn (4) to ensure charge neutrality.

$$\frac{m^+}{m^-} = \frac{Q_s^-}{Q_s^+}\left(\frac{\Delta V^-}{\Delta V^+}\right) \quad (4)$$

In the equation m^+, ΔV^+ and Q_s^+ represents the mass active material, potential range, and the specific capacity of the positive electrode, respectively; (variables with (−) correspond to the components of the negative electrode).

The asymmetric device is systematically illustrated in Scheme 2 to show the various components that build up the device, including the cathode, anode, electrolyte, and the separating membrane.

The CV curves of the device at a scan rate of 100 mV s^{-1} across different potential windows (1.0–1.6 V) are displayed in Fig. 5(a). It is evident that at lower potential windows (1.0–1.4 V),

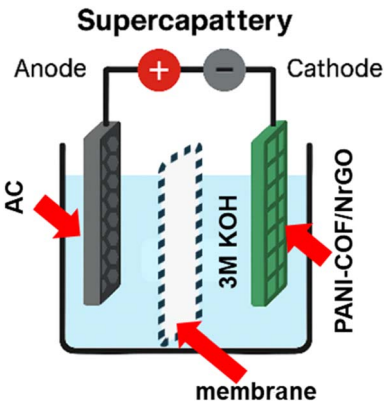

Scheme 2 Illustration of the supercapattery device.

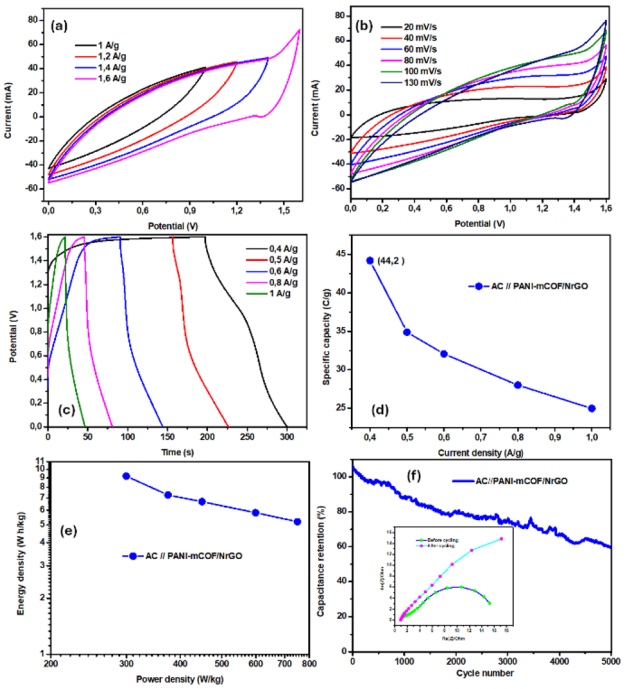

Fig. 5 (a) CV curves of the AC//PANI-COF/NrGO at various potential windows (constant 20 mV s^{-1}), (b) CV curves of the AC//PANI-COF/NrGO at various scan rates, (c) GCD curves of the asymmetric device at various current densities, (d) specific capacity *vs.* current density of the device, (e) ragone plot of the AC//PANI-COF/NrGO device, and (f) cycling stability testing of the device (insert: EIS before and after cycling).

the device displayed nearly rectangular CV profiles, characteristic of electric double-layer capacitance (EDLC) behavior dominated by the AC anode. However, when the potential window was extended to 1.6 V, clear redox peaks emerged, which can be attributed to the faradaic contribution from the PANI-COF/NrGO cathode. This demonstrates the hybrid charge storage mechanism of the device, combining both EDLC from AC and battery-type from the redox-active PANI and COF, thereby justifying its classification as a supercapattery device.[51] The rate performance of the device was further investigated by CV at scan rates ranging from 20 to 130 mV s^{-1} (Fig. 5(b)). The CV curves retained their overall shape with minimal distortion even at higher scan rates, reflecting the excellent ion diffusion kinetics and electrical conductivity of the composite. This suggests that the interconnected porous structure of the COF and the conductive NrGO backbone facilitated efficient charge transport, while PANI contributed to fast and reversible redox reactions.[52] The GCD profiles of the supercapattery device at current densities from 0.4 to 1 A g^{-1} are shown in Fig. 5(c). The device delivered a specific capacity of 44.19 C g^{-1} at 0.4 A g^{-1}, which gradually decreased to 24.97 C g^{-1} at 1 A g^{-1} (Fig. 5(d)), corresponding to a retention of more than 56% of the initial capacity. This relatively high-capacity retention under increased current density highlights the synergistic effect of the composite electrode, where NrGO ensures high conductivity, PANI provides rapid redox activity, and COF offers ion-accessible porosity.[53] The Ragone plot (Fig. 5(e)) revealed that the AC//PANI-COF/NrGO device achieved an energy density of 9.2 Wh kg^{-1} at a power density of 300 W kg^{-1}, surpassing several previously reported COF- and PANI-based electrode systems (as benchmarked in Table 5). Such performance reflects the efficient energy–power balancing of the device, making it attractive for high-power energy storage applications. Finally, the long-term cycling stability of the supercapattery device was evaluated over 5000 charge/discharge cycles at a fixed current density. As shown in Fig. 5(f), the device retained approximately 60% of its initial capacity, indicating reasonable durability. The partial capacity fade could be associated with the volumetric expansion/contraction of PANI during repeated redox cycling, which is a well-known limitation of conducting polymers.[54] Furthermore, the Nyquist plots of the AC//PANI-COF/NrGO device before and after 5000 charge–discharge cycles are shown in Fig. 5(f) insert, with notable changes. Before cycling, the semicircle at high frequency is relatively small, indicating low charge-transfer resistance and efficient electron transfer at the electrode–electrolyte interface. After 5000 cycles, the semicircle increases in diameter, suggesting a moderate increase in charge-transfer resistance (likely due to slight structural or interfacial changes during long-term cycling).[55] The assembled device demonstrates the potential of PANI-COF/NrGO battery-type electrode as a high-performance cathode material for hybrid devices, combining high energy density with good rate performance and moderate cycling stability.

Table 5 Comparison of the PANI-COF/NrGO composite with other reported electrode materials in a two-electrode system

Electrode material	Energy density (Wh kg^{-1})	Power density (W kg^{-1})	Ref.
Pani/rGO//CNF	0.6	300	49
Pani/rGO//MWCNT	2.4	350	49
Pani/rGO//PMAC	7.9	325	49
PANI-$ZnCo_2O_4$//AC	13.25	375	56
rGO/MXene-PPy//rGO/MXene-PPy	11.3	500	57
4KT-Tp COF	12.5	240	58
AC//NWNU-COF-4	14.85	394.83	48
AC//PANI-COF/NrGO	9.2	300	This work

Conclusions

This work focused on a ternary composite based on COF/NrGO composite wrapped with PANI to produce PANI-COF/NrGO composite. The successful preparation of the PANI-COF/NrGO composite was confirmed using XRD, FTIR, TGA, BET, and SEM analytical techniques. Furthermore, the electrochemical performance of the prepared materials was evaluated using CV, GCD, and EIS, and the prepared electrode materials (PANI, PANI-COF, and PANI-COF/NrGO) exhibited battery-type storage behaviour in 3 mol L^{-1} KOH at a potential window of 0.5 V *vs.* Ag/AgCl. The PANI-COF/NrGO composite has shown superior specific capacities of 409.79 (scan rate: 20 mV s^{-1}) and 410 C g^{-1} (current density: 2 A g^{-1}) calculated using CV and GCD, respectively. The PANI-COF/NrGO composite exhibited higher electrochemical performance compared to its precursors and was further used as an electrode material in an asymmetric supercapattery device. The asymmetric device was constructed using PANI-COF/NrGO composite as a positive electrode and AC as a negative electrode. The device displayed a specific capacity of 44.2 C g^{-1} at a current density of 0.4 A g^{-1} and delivered an energy density of 9.2 Wh kg^{-1} at a power density of 300 W kg^{-1}. The PANI wrapped composite has shown impressive electrochemical performance, and it may be used as a promising electrode material for developing new generation energy storage devices (*i.e.*, supercapatteries, batteries, and supercapacitors).

Author contributions

Daniel M. Teffu: writing – original draft, investigation, formal analysis, data curation. Kwena D. Modibane: writing – review & editing, supervision, funding acquisition, project administration formal analysis, conceptualization. Katlego Makgopa: writing – review & editing, supervision, project administration, conceptualization.

Conflicts of interest

The authors declare that they have no known competing financial interests or personal relationships that could have appeared to influence the work reported in this paper.

Data availability

Data will be made available on request.

Acknowledgements

The authors would like to acknowledge the University of Limpopo, Tshwane University of Technology, DSI/NRF SARChI Chair-150531 Grant No. RCGH22082353005, NRF-Competitive Support for Unrated Researchers (Grant No. SRUG2205035936 and UID No. 138085) for financial support. DMT would like to acknowledge the NRF-Sasol Doctoral Scholarship (UID No. 140469).

Notes and references

1 R. Aridi, M. Aridi, M-L. Pannier and T. Lemenand, Eco-environmental, and social impacts of producing electricity with various renewable energy sources, *Energy*, 2025, **320**, 135139, DOI: 10.1016/j.energy.2025.135139.
2 Y. A. Solangi and C. Magazzino, Evaluating financial implications of renewable energy for climate action and sustainable development goals, *Renewable Sustainable Energy Rev.*, 2025, **212**, 115390, DOI: 10.1016/j.rser.2025.115390.
3 M. Ibrahim, Z. Wen, X. Sun and H. N. Abdelhamid, *In situ* polymerization of a melamine-based microsphere into 3D nickel foam for supercapacitors, *RSC Adv.*, 2024, **14**, 5566, DOI: 10.1039/D3RA08489B.
4 M. Arun, S. Samal, D. Barik, S. S. R. Chandran, K. Tudu and S. Praveenkumar, Integration of energy storage systems and grid modernization for reliable urban power management toward future energy sustainability, *J. Energy Storage*, 2025, **114**, 115830, DOI: 10.1016/j.est.2025.115830.
5 C. V. V. Muralee Gopi, S. Alzahmi, V. Narayanaswamy, R. Vinodh, B. Issa and I. M. Obaidat, Supercapacitors: A promising solution for sustainable energy storage and diverse applications, *J. Energy Storage*, 2025, **114**, 115729, DOI: 10.1016/j.est.2025.115729.
6 A. Singh, et al., Advancements in wearable energy storage devices *via* fabric-based flexible supercapacitors, *J. Energy Storage*, 2025, **109**, 115183, DOI: 10.1016/j.est.2024.115183.
7 A. A. Mirghni, et al., Designing coin-cell supercapacitors: Combining graphene foam with metal oxide composite electrodes for improved energy storage performance, *FlatChem*, 2025, **50**, 100829, DOI: 10.1016/j.flatc.2025.100829.
8 K. Makgopa, M. S. Ratsoma and K. D. Modibane, Intrinsic properties of metal–organic frameworks (MOFs) in supercapacitor applications, *Curr. Opin. Electrochem.*, 2022, **36**, 101112, DOI: 10.1016/j.coelec.2022.101112.
9 D. M. Teffu, et al., Interrogation of Electrochemical Performance of Reduced Graphene Oxide/Metal-organic Framework Hybrid for Asymmetric Supercabattery Application, *Electroanalysis*, 2020, **32**, 2827, DOI: 10.1002/elan.202060303.
10 A. Ali, S. Ahmed, W. Jiang, G. Park and S. J. Oh, Harnessing MOF intrinsic properties for enhanced supercapacitor performance, *Curr. Opin. Electrochem.*, 2025, **50**, 101640, DOI: 10.1016/j.coelec.2024.101640.
11 K. Makgopa, M. S. Ratsoma, K. Raju, L. F. Mabena and K. D. Modibane, One-Step Hydrothermal Synthesis of Nitrogen-Doped Reduced Graphene Oxide/Hausmannite Manganese Oxide for Symmetric and Asymmetric Pseudocapacitors, *ACS Omega*, 2021, **6**, 31421, DOI: 10.1021/acsomega.1c02302.
12 Y. Liu, Q. Jin, S. Hu and Z. Qin, High mass loading of sulfonated holey graphene/PANI in situ growing on carbon cloth for superior areal capacitance of flexible

supercapacitor, *Mater. Today Chem.*, 2025, **43**, 102514, DOI: 10.1016/j.mtchem.2025.102514.
13 D. M. Teffu, et al., Metal and covalent organic frameworks (MOFs and COFs): A comprehensive overview of their synthesis, characterization and enhanced supercapacitor performance, *Coord. Chem. Rev.*, 2025, **540**, 216798, DOI: 10.1016/j.ccr.2025.216798.
14 X. Li, K. Kawai, M. Fujitsuka and Y. Osakada, COF-based photocatalyst for energy and environment applications, *Surf. Interfaces*, 2021, **25**, 101249, DOI: 10.1016/j.surfin.2021.101249.
15 N. An, et al., A novel COF/MXene film electrode with fast redox kinetics for high-performance flexible supercapacitor, *Chem. Eng. J.*, 2023, **458**, 141434, DOI: 10.1016/j.cej.2023.141434.
16 S. Haldar, et al., Incorporating Conducting Polypyrrole into a Polyimide COF for Carbon-Free Ultra-High Energy Supercapacitor, *Adv. Energy Mater.*, 2022, **12**, 2200754, DOI: 10.1002/aenm.202200754.
17 Z. Zhang, et al., Exquisitely functionalized porphyrin-COF self-supporting nanofilm for high-performance in-plane micro-supercapacitor, *Appl. Surf. Sci.*, 2025, **680**, 161327, DOI: 10.1016/j.apsusc.2024.161327.
18 C. Li et al., *Pristine MOF and COF Materials for Advanced Batteries*, Oct. 01, Elsevier B.V., 2020, DOI: 10.1016/j.ensm.2020.06.005.
19 M. A. Deyab and G. Mele, PANI@Co-Porphyrins composite for the construction of supercapacitors, *J. Energy Storage*, 2019, **26**, 101013, DOI: 10.1016/j.est.2019.101013.
20 M. I. Bashir, F. Anjum, M. Imran, H. M. Fahad and F. Sher, Facile synthesis of hybrid electrode by bimetallic MOFs/polyaniline composite for high-performance asymmetric supercapacitors, *J. Mater. Sci.: Mater. Electron.*, 2024, **35**, 742, DOI: 10.1007/s10854-024-12496-6.
21 C. Peng, H. Yang, S. Chen and L. Wang, Supercapacitors based on three-dimensional porous carbon/covalent-organic framework/polyaniline array composites, *J. Energy Storage*, 2020, **32**, 101786, DOI: 10.1016/j.est.2020.101786.
22 M. Ibrahim, M. G. Fayed, S. G. Mohamed, Z. Wen, X. Sun and H. N. Abdelhamid, High-Performance Lithium-Ion Battery and Supercapacitors Using Covalent Organic Frameworks (COFs)/Graphitic Carbon Nitride ($g\text{-}C_3N_4$)-Derived Hierarchical N-Doped Carbon, *ACS Appl. Energy Mater.*, 2022, **5**, 12828–12836, DOI: 10.1021/acsaem.2c02415.
23 M. Kamalabadi, S. Khalili, T. Madrakian and A. Afkhami, Facile synthesis of magnetic melamine-based covalent organic framework for removal of Amido Black 10B, *Eur. Phys. J. Plus*, 2022, **137**, 544, DOI: 10.1140/epjp/s13360-022-02758-9.
24 M. S. Ratsoma, et al., Investigation of N-rGO/NH4MnPO4·H2O as battery-type electrode material for high-performance supercapatteries, *Electrochim. Acta*, 2025, **524**, 146079, DOI: 10.1016/j.electacta.2025.146079.
25 N. M. Musyoka, J. Ren, H. W. Langmi, B. C. North, M. Mathe and D. Bessarabov, Synthesis of rGO/Zr-MOF composite for hydrogen storage application, *J. Alloys Compd.*, 2017, **724**, 450, DOI: 10.1016/j.jallcom.2017.07.040.
26 K. E. Ramohlola, et al., Polyaniline-metal organic framework nanocomposite as an efficient electrocatalyst for hydrogen evolution reaction, *Composites, Part B*, 2018, **137**, 129, DOI: 10.1016/j.compositesb.2017.11.016.
27 V. M. Moagi, M. V. Maphoru and L. F. Mabena, Preparation, characterisation, and electrochemical evaluation of nickel sulphide on lignin-derived carbon material for supercapacitors, *Electrochim. Acta*, 2025, **540**, 147019, DOI: 10.1016/j.electacta.2025.147019.
28 G. Qiu, A. Zhu and C. Zhang, Hierarchically structured carbon nanotube–polyaniline nanobrushes for corrosion protection over a wide pH range, *RSC Adv.*, 2017, **7**, 35330, DOI: 10.1039/C7RA05235A.
29 K. E. Ramohlola, K. D. Modibane, M. M. Ndipingwi, E. Makhado, M. J. Hato, S. Raseale, K. Makgopa and E. I. Iwuoha, The effect of copolymerization on the electrocatalytic hydrogen evolution properties of polyaniline in acidic medium, *Discover Mater.*, 2025, **5**, 170, DOI: 10.1007/s43939-025-00366-9.
30 K. Banjerdteerakul, H. Peng and K. Li, Covalent organic frameworks based membranes for separation of azeotropic solvent mixtures by pervaporation, *J. Membr. Sci.*, 2023, **678**, 121679, DOI: 10.1016/j.memsci.2023.121679.
31 H. Abdali and A. Ajji, Preparation of Electrospun Nanocomposite Nanofibers of Polyaniline/Poly(methyl methacrylate) with Amino-Functionalized Graphene, *Polymers*, 2017, **9**, 453, DOI: 10.3390/polym9090453.
32 M. Rani, B. Zaheer, F. Sajid, A. Ibrahim, A. A. Shah and A. D. Chandio, A Novel Hybrid Composite of Co-MOF@GO/PANI: Synthesis and Electrochemical Evaluation as an Electrode Material for Supercapacitors, *J. Inorg. Organomet. Polym. Mater.*, 2025, DOI: 10.1007/s10904-025-03879-1.
33 F. Sun, et al., Enhanced electrochemical performance by polyaniline (PANI) on covalent organic framework - Carbon nanotube (COF-CNT) as cathode catalyst for microbial fuel cells, *Int. J. Hydrogen Energy*, 2024, **55**, 665, DOI: 10.1016/j.ijhydene.2023.11.189.
34 A. P. Mahajan, S. B. Kondawar, R. P. Mahore, B. H. Meshram and P. D. Virutkar, Polyaniline/MnO2 Nanocomposites Based Stainless Steel Electrode Modified Enzymatic Urease Biosensor, *Procedia Mater. Sci.*, 2015, **10**, 699, DOI: 10.1016/j.mspro.2015.06.075.
35 T. C. Maponya, K. D. Modibane, T. R. Somo and K. Makgopa, Selective adsorption of palladium ions from wastewater by ion-imprinted MIL-101(Cr) derived from waste polyethylene terephthalate: Isotherms and kinetics, *Sep. Purif. Technol.*, 2023, **307**, 122767, DOI: 10.1016/j.seppur.2022.122767.
36 T. C. Maponya, K. Makgopa, T. R. Somo, D. M. Tshwane and K. D. Modibane, Highly adsorptive removal of palladium and platinum ions from wastewater using novel ethylenediamine-glutaraldehyde-grafted metal organic framework, *Environ. Nanotechnol., Monit. Manage.*, 2023, **20**, 100805, DOI: 10.1016/j.enmm.2023.100805.
37 S. Gopukumar, K. Y. Chung and K. B. Kim, Novel synthesis of layered LiNi1/2Mn1/2O2 as cathode material for lithium

rechargeable cells, *Electrochim. Acta*, 2004, **49**, 803, DOI: 10.1016/j.electacta.2003.09.034.

38 R. Zhang, Y. Li, Y. Ci, F. Li, T. Chen and Y. Tang, Synthesis and characterization of polyaniline-based composites using cellulose nanocrystals as biological templates, *Int. J. Biol. Macromol.*, 2024, **269**, 132098, DOI: 10.1016/j.ijbiomac.2024.132098.

39 M. Beygisangchin, S. Abdul Rashid, S. Shafie and A. R. Sadrolhosseini, Polyaniline Synthesized by Different Dopants for Fluorene Detection *via* Photoluminescence Spectroscopy, *Materials*, 2021, **14**, 7382, DOI: 10.3390/ma14237382.

40 S. Nawaz, et al., Polyaniline inside the pores of high surface area mesoporous silicon as composite electrode material for supercapacitors, *RSC Adv.*, 2022, **12**(27), 17228–17236, DOI: 10.1039/D2RA01829B.

41 C. Van Tran, et al., Enhanced photocatalytic performance of polyaniline nanoparticles for efficient dye degradation under simulated sunlight, *Nanoscale Adv.*, 2025, **7**, 800, DOI: 10.1039/D4NA00707G.

42 X. Yan, Z. Tai, J. Chen and Q. Xue, Fabrication of carbon nanofiber–polyaniline composite flexible paper for supercapacitor, *Nanoscale*, 2011, **3**, 212, DOI: 10.1039/C0NR00470G.

43 S. M. Abdullah, et al., Tailoring NiCoCu layered double hydroxide with Ag-citrate/polyaniline/functionalized SWCNTs nanocomposites for supercapacitor applications, *RSC Adv.*, 2024, **14**, 14438, DOI: 10.1039/D4RA01324G.

44 J.-J. Zhou, et al., Boosting Specific Capacity for Supercapattery by *In Situ* Formation of Amorphous Ni–Co–Borate on MOF-Derived Ni–Co–LDH Nanosheet Array, *ACS Appl. Energy Mater.*, 2020, **3**, 12046, DOI: 10.1021/acsaem.0c02181.

45 A. Umar, et al., Exploring the potential of reduced graphene oxide/polyaniline (rGO@PANI) nanocomposites for high-performance supercapacitor application, *Electrochim. Acta*, 2024, **479**, 143743, DOI: 10.1016/j.electacta.2023.143743.

46 S. Liu, et al., All-organic covalent organic framework/polyaniline composites as stable electrode for high-performance supercapacitors, *Mater. Lett.*, 2019, **236**, 354, DOI: 10.1016/j.matlet.2018.10.131.

47 A. F. M. EL-Mahdy, et al., Synthesis of [3 + 3] β-ketoenamine-tethered covalent organic frameworks (COFs) for high-performance supercapacitance and CO2 storage, *J. Taiwan Inst. Chem. Eng.*, 2019, **103**, 199, DOI: 10.1016/j.jtice.2019.07.016.

48 H. Guo, et al., A new COF linked by an ether linkage (–O–): synthesis, characterization and application in supercapacitance, *RSC Adv.*, 2019, **9**, 13458, DOI: 10.1039/C9RA01357A.

49 B. Burentogtokh, B. Batsuren, S. Galsan and A. Pagvajav, Polyaniline/Reduced Graphene Oxide Composite as an Electrode for Symmetric and Asymmetric Supercapacitors, *J. Appl. Polym. Sci.*, 2025, **142**, 17, DOI: 10.1002/app.56785.

50 H. Shao, Z. Lin, K. Xu, P.-L. Taberna and P. Simon, Electrochemical study of pseudocapacitive behavior of Ti3C2Tx MXene material in aqueous electrolytes, *Energy Storage Mater.*, 2019, **18**, 456, DOI: 10.1016/j.ensm.2018.12.017.

51 Y. Luo, K. Gu, T. Yang and M. Zhang, Synthesis of porous nanosheet Co3O4 with two pairs of redox peaks for high performance as a battery electrode, *J. Energy Storage*, 2019, **21**, 362, DOI: 10.1016/j.est.2018.12.008.

52 Y. Yang, et al., Anthraquinone-based covalent organic framework/reduced graphene oxide composites for supercapacitors, *J. Energy Storage*, 2025, **131**, 115881, DOI: 10.1016/j.est.2025.115881.

53 M. K. Sahoo, P. Mane, B. Chakraborty and J. N. Behera, Three-Dimensional Ni-MOF as a High-Performance Supercapacitor Anode Material; Experimental and Theoretical Insight, *Inorg. Chem.*, 2024, **63**, 6383, DOI: 10.1021/acs.inorgchem.4c00144.

54 M. Z. Iqbal, et al., Exploring MOF-199 composites as redox-active materials for hybrid battery-supercapacitor devices, *RSC Adv.*, 2023, **13**, 2860, DOI: 10.1039/D2RA06457J.

55 A. E. Elkholy, A. S. Dhmees, F. E.-T. Heakal and M. A. Deyab, Mesoporous $ZnMoS_4$ as a supercapacitor electrode material with battery-like behavior, *New J. Chem.*, 2019, **43**, 1987, DOI: 10.1039/C8NJ05640D.

56 F. S. Omar, A. Numan, N. Duraisamy, S. Bashir, K. Ramesh and S. Ramesh, A promising binary nanocomposite of zinc cobaltite intercalated with polyaniline for supercapacitor and hydrazine sensor, *J. Alloys Compd.*, 2017, **716**, 96, DOI: 10.1016/j.jallcom.2017.05.039.

57 G. Wang, N. Jiang, Y. Xu, Z. Zhang, G. Wang and K. Cheng, Solvent-assisted assembly of reduced graphene oxide/MXene-polypyrrole composite film for flexible supercapacitors, *J. Colloid Interface Sci.*, 2023, **630**, 817, DOI: 10.1016/j.jcis.2022.10.135.

58 M. Li, et al., Skeleton Engineering of Isostructural 2D Covalent Organic Frameworks: Orthoquinone Redox-Active Sites Enhanced Energy Storage, *CCS Chem.*, 2021, **3**(2), 696, DOI: 10.31635/ccschem.020.202000257.